Published on 12 December 2014. Downloaded by Changchun Institute of Optics, Fine Mechanics and Physics, CAS on 29/05/2016 14:28:41.

RSC Advances

REVIEW

View Article Online
View Journal | View Issue

Cite this: *RSC Adv.*, 2015, **5**, 7267

Metal/metal oxide nanostructures derived from metal–organic frameworks

Yonghai Song,[a] Xia Li,[a] Lanlan Sun[b] and Li Wang*[a]

Received 13th October 2014
Accepted 12th December 2014

DOI: 10.1039/c4ra12273a

www.rsc.org/advances

Metal–organic frameworks (MOFs) have important potential applications in gas separation, storage and purification, and also for use as electrode materials, catalysts, sensors and in drug-delivery systems. There has been increasing interest in the synthesis of micro- and nanostructures based on MOFs, particularly on the improvement of their versatility and the simplification of synthesis procedures. This paper reviews the use of MOFs as matrices for solid-state decomposition and in the synthesis of metal/metal oxide micro- and nanostructures, porous carbon and composite materials.

1. Introduction

Nanoscale materials are very different from the corresponding bulk materials and have special properties, such as an extremely small size, quantum effects and a large specific surface area. With the development of nanoscience and technology, metal oxide nanostructures (MONs) have attracted increasing attention. Metal–organic frameworks (MOFs) have been used to synthesize a variety of metal/MONs (M/MONs) that are of interest in many applications related to porosity and secondary building units.

MOFs consist of transition metal ions or clusters of metal ions occupying the nodal positions in a crystalline framework and held in place by bi- or multi-nodal rigid organic linkers (Fig. 1). The term coordination polymer is used as a synonym for MOFs.[1] MOFs have been developed very quickly, not only in terms of their broad range of structures, topologies and compositions, but also in their potential applications. Their special properties (*e.g.* a low-density porous structure, high

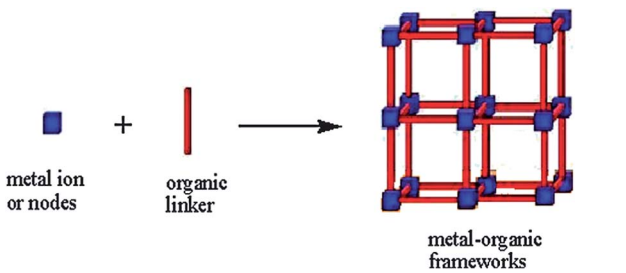

Fig. 1 Components and structure of MOFs. Reproduced with permission from Dhakshinamoorthy *et al.*,[5] *Chem. Soc. Rev.*, 2012, **41**. Copyright The Royal Society of Chemistry (2012).

[a]*Key Laboratory of Functional Small Organic Molecule, Ministry of Education, College of Chemistry and Chemical Engineering, Jiangxi Normal University, Nanchang 330022, China. E-mail: yhsonggroup@hotmail.com; lwanggroup@aliyun.com; Fax: +86 791 88120862; Tel: +86 791 88120862*

[b]*State Key Laboratory of Luminescence and Applications, Changchun Institute of Optics, Fine Mechanics and Physics, Chinese Academy of Sciences, 3888 East Nan-Hu Road, Changchun 130033, China*

Yonghai Song received his PhD in analytical chemistry from the Changchun Institute of Applied Chemistry, Chinese Academy of Science, China. He is currently working as a professor at Jiangxi Normal University. His current research interests focus on nanomaterials and their applications in biosensors.

Xia Li received her BSc degree in chemistry in 2012 from Jiangxi Technology Normal University, China. She is working toward her master's degree in Jiangxi Normal University, China. Her research interests are nanomaterials and their applications in sensors.

Published on 12 December 2014. Downloaded by Changchun Institute of Optics, Fine Mechanics and Physics, CAS on 29/05/2016 14:28:41.

surface area, hybrid features and tunable porosity) have led to their application in gas separation and storage,[2] sensors, catalysis[3] and in drug storage and drug-delivery systems.[4] There are a number of advantages in using MOFs as precursors to synthesize M/MMONs: (1) there are a large number of MOFs of different compositions, morphologies and structures; (2) MOFs have a flexible structure that behaves dynamically and responds to external factors, such as the presence of guest molecules and changes in temperature or pressure; (3) MOFs allow the entry and polymerization of additional precursors inside the pores, similar to mesoporous silica and zeolites; (4) MOFs consist of inorganic clusters and organic linkers, leading to a relatively low stability; and (5) the size and pore structure of MOFs are controllable.

Several reviews have been published on applications[6] and methodologies for the synthesis of MOFs and the encapsulation of active species in MOFs.[7–9] However, a review of the methods of synthesis and applications of M/MMONs has not yet been published. This paper reviews the literature and gives an accessible summary of this field, including various synthetic approaches and applications of the derived materials. This field is at a stage where trends in synthetic approaches can be identified and applications are becoming more diverse. Some challenges have been identified that suggest long-term research directions.

2. Synthesis of M/MMONs

The rational synthesis of well-defined MONs with uniform dimensions and controlled architectures is very important in adjusting their chemical and physical properties. This is because the electronic structure, bonding, surface energy and chemical reactivity of these materials are directly related to their surface morphology. There have been tremendous advances in the last two decades in the synthesis of size- and morphology-controlled metal oxides using chemical methods. However, there are still many challenges in creating nanostructures with particular morphologies and in exploring well-controlled methods. Using the MOF template pyrolysis route, we can obtain the desired product without agglomeration, avoiding the complex aqueous chemistry and multistep processes that often lead to impurities. More importantly, this method is practical for forming metal oxide micro/nanostructures with various controlled shapes, including microplates,[10] nanowires,[11] nanorods, nanoparticles,[12] spongy shapes,[13] nanosheets[14] and hollow[15] and coralloid nanostructures.[16] This can be achieved by controlling reaction conditions such as the temperature and reaction time, and the precursors. Recent reports on metal/metal oxide structures derived from MOFs have focused on Cu/CuO, Co/Co_3O_4, ZnO, Fe_2O_3/Fe_3O_4, CdO, MnO and InO. As a result of their porosity and the broad range of structures and compositions of matrix MOFs, the as-synthesized metal oxide materials have specific morphologies and tunable nanocrystalline frameworks.

2.1 Cu/CuO

Pure Cu/CuO metal/metal oxide structures with hollow, spongy, coralloid and spherical shapes have been synthesized using $Cu_3(BTC)_2$, a well-known Cu–MOF (also called HKUST-1; BTC = benzene-1,3,5-tricarboxylato) as the template. Using the same template, CuO/CeO_2 composites with high catalytic activity have also been synthesized when loaded with a Ce precursor. The thermogravimetric analysis (TGA) curve of $Cu_3(BTC)_2$ in Fig. 2a shows that MOFs undergo considerable weight loss on heating to 300 °C as a result of the decomposition of organic ligands. Wu *et al.*[15] successfully synthesized porous CuO hollow octahedral structures using $Cu_3(BTC)_2$ as a template and heating at 300 °C in nitrogen gas, followed by annealing at the same temperature in an air flow. In the heating step, the carbon generated during calcination may have acted as a temporary buffer, preventing further contraction of the MOFs. In the annealing step, the air flow oxidized and removed the carbon to form the porous material. Why the product showed a hollow morphology was unknown. However, in a similar study,[17] a calcination method was used to prepare hollow CuO/Cu_2O polyhedrons and the mechanism of formation of the hollow structures deduced in this work might explain the work of Wu *et al.*[15] $Cu_3(BTC)_2$ polyhedrons were heated at 350 °C based on the TGA results and it was deduced that a thin intermediate shell was formed on the surface of the precursor polyhedron at the start of the thermal oxidation process. This thin layer acted as an interface to separate the inner $Cu_3(BTC)_2$ from

Li Wang received her PhD in analytical chemistry from the Changchun Institute of Applied Chemistry, Chinese Academy of Sciences, China. She is currently working as a professor at Jiangxi Normal University. Her current research interest is focused on nanomaterials and their applications in biosensors and supercapacitors.

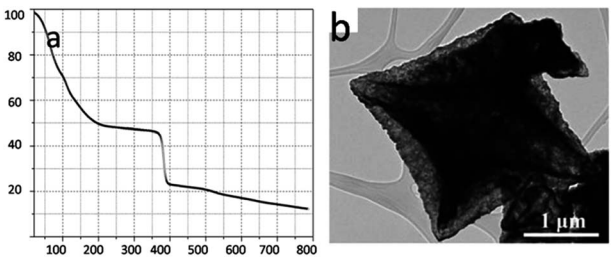

Fig. 2 (a) TGA curve of as-synthesized Cu–BTC MOF precursor microcrystals at a heating rate of 10 °C min^{-1} in a flow of N_2 gas. (b) TEM image of hollow octahedral of CuO. Reproduced with permission from R. Wu *et al.*,[15] *J. Mater. Chem. A*, 2013, **1**. Copyright The Royal Society of Chemistry (2013).

 This journal is © The Royal Society of Chemistry 2015

Published on 12 December 2014. Downloaded by Changchun Institute of Optics, Fine Mechanics and Physics, CAS on 29/05/2016 14:28:41.

atmospheric oxygen. However, the interface consisted of an intermediate shell with many vacancies, which allowed $Cu_3(BTC)_2$ to diffuse out. The diffusion rate of $Cu_3(BTC)_2$ is greater than that of atmospheric oxygen during the oxidation reactions and voids are therefore generated, which eventually results in a hollow cavity (Fig. 2b). This diffusion behavior has been referred to as the Kirkendall effect.

Table 1 lists other kinds of specifically shaped Cu/CuO structures derived from MOFs. The synthesis of Cu from MOFs must take place under the protection of an inert gas or without the circulation of air. Chen *et al.*[16] realized the transformation of HKUST-1 into symmetrical coralloid three-dimensional Cu microstructures in a tube closed at one end at 500 °C. At 500 °C in air, this coralloid Cu was converted from Cu to CuO *in situ* and the morphology remained unchanged. The formation of Cu is a result of the high reduction potential of Cu^{2+} in MOFs and the ease with which the atmosphere is reduced. This phenomenon has been widely reported and is illustrated in later sections.

The kinds of Cu–MOFs used as precursors for the synthesis of Cu/CuO have so far been limited. As Cu is such an important transition metal, more research should be carried out on MOFs containing Cu ions.

2.2 ZnO

With our deepening understanding of MOFs, it has been found that the highly dispersed ordered metal ions separated by organic linkers in MOFs are not only good precursors for preparing well-shaped M/MONs, but also ideal candidates for metal oxide quantum dot (QD) materials. MOF-5 [also known as IRMOF-1; $Zn(BTC)_x$] is chosen as a case study as a result of its semiconductor and luminescence behavior arising from ZnO QDs. Yang *et al.*[18] synthesized ZnO QDs without intrinsic defects or agglomeration that were embedded in hierarchical porous carbon matrices by heat-treated IRMOF-1 at 550 °C under nitrogen at a heating rate of 10 °C min^{-1}. This unique microstructure had an outstanding electrochemical performance (capacity, cyclability, and rate of charge and discharge) when evaluated as an anode material for lithium ion batteries (LIBs). A temperature-programmed mass spectrometry (TP-MS) study of the gas and liquid products formed during the decomposition of MOF-5 indicated that the products of MOF-5 decomposition were CO_2, benzene and C/ZnO nanoparticles, in which the ZnO was covered by amorphous carbon. Fig. 3 shows the proposed decomposition mechanism of MOF-5. There are three types of breaking of the carboxylic bridges: (a) Zn–O bond-breaking between the Zn_4O cluster and the carboxylic group; (b) O–C bond-breaking of the carboxylic group; and (c) C–C bond-breaking between the carboxylic group and the benzene ring. When the breakage occurred at positions (a) and (c), CO_2 molecules and C_6H_4 intermediates were formed. The C_6H_4 intermediates then connected to each other to form amorphous carbon with the release of some hydrogen. At the same time, one C_6H_4 intermediate was able to accept two hydrogen atoms to form a benzene molecule. The Zn_4O clusters did not obtain any oxygen atoms from a carboxylic group in this mode of bond-breaking. In contrast, if the carboxylic bridges broke at position (b), a C–C_6H_4–C intermediate was formed and Zn_4O obtained two oxygen atoms. To form a stoichiometric ZnO product, each Zn_4O only needed 1.5 bridges to be broken at position (b). Because each Zn_4O cluster had six carboxylic bridges, the formation of crystalline ZnO particles in the decomposition of MOF-5 indicated that 4.5 bridges (75% of six bridges) were broken at positions (a) and (c) and 1.5 bridges (25% of six bridges) were broken at position (b).

The number of different MOFs used as precursors to form ZnO is more than that for the transformation of MOFs into Cu/CuO. In addition to MOF-5,[20–22] $Zn_3(NTA)_2$ (NTA = nitrilotriacetic), $Zn(TDA)H_2O$[23] [TDA = $S(CHCOO)_2^{2-}$], Zn–MOF with amino acids as organic linkers[24] and many other MOFs[24,25] have been used. However, although the organic linkers will eventually decompose and volatilize, the influence of different ligands of precursor MOFs on the morphology of the product should not be neglected. For example, ZnO rings were synthesized from MOFs with *N*,*N*′-phenylenebis(salicylideneimine)-dicarboxylic acid and 1,4-benzendicarboxylic acid linkers. The MOFs using TDA or 2,2′-bipyridine-4,4′-dicarboxylic acid as ligands realized the transformation into ZnO flakes and micro-particles. The same ligands affected the crystal structure of the product metal oxide if the MOFs were synthesized under different conditions. This may be a result of different spatial structures. Nitrilotriacetic acid (H_3NTA) reacts in the solid phase with zinc hydroxide (1 : 1) to form three-dimensional ladder-like MOFs that transform wurtzite (ZnO) nanoparticles when heated to >600 °C. Another mixed coordination network was formed with an excess of Zn^{2+} hydroxide, which, on decomposition at about 500 °C, formed microwires of ZnO (Fig. 4a and b).[20]

We can learn this distinction through structural analysis. The previous method resulted in a coordination polymer that looked like an array of zinc-containing metallo-macrocyclic molecules containing hexa-coordinated Zn^{2+} with a distorted octahedral geometry.[20] Fig. 5a shows that three of the coordination sites were occupied by water molecules, two were bonded to the ligand and the remaining site was occupied by the tertiary amine bridgehead N-atom of the ligand. The compound synthesized in the second method was a dimeric Zn nitrilotriacetato complex containing the hexa-aquazinc(II) cation, the dimeric Zn–NTA complex anion and with water in the crystal lattice. Fig. 5b shows that there were three symmetry-independent Zn sites in the structure. The first two (Zn1 and Zn2) were distorted octahedral sites with five carboxyl oxygen atoms and one amine nitrogen making up the coordination environment. The other zinc cation, Zn3, was coordinated to six water molecules. Although the mechanism of how the spatial structure worked in the growth of metal oxides was not determined, a unique correlation between the size of the nanoparticles and the distance between the secondary building units inside the MOF precursors was demonstrated.

This theory was further confirmed by the thermolysis of Co–MOFs and Cu–MOFs.[30] It was shown that the Cu and CuO particles synthesized by the thermolysis of three-dimensional $[Cu_3(TMA)_2(H_2O)_3]_n$ were larger than the particles synthesized from two-dimensional $[Cu_2(hfbba)_2(3\text{-mepy})_2]\cdot(DMF)_2(3\text{-mepy})$.

Published on 12 December 2014. Downloaded by Changchun Institute of Optics, Fine Mechanics and Physics, CAS on 29/05/2016 14:28:41.

Table 1 Metal oxides derived from MOFs and their applications

MOF[a]	Target temperature (°C), rate (°C min^{-1})	Atmosphere	Product and morphology	Application	Ref.
Zn(TDA)H_2O	>500, —	—	Sponge-like ZnO	—	23
$Mn_{12}O_{12}(O_2CR)_{16}(H_2O)_4$ (R = C_6H_5, CH_3, and $C_6H_5OCH_2$)	400/500/600	Air	Novel MnO nano- and microscale particles	—	66
Zn-MOF	550, —	—	Hexagonal rings of ZnO	—	25
$Zn_4O(BDC)_4$	480, 10	Vacuum	Sphere-shaped ZnO@C	—	19
$Zn_4O(BDC)_4$	900, 10	Air	ZnO	—	
MOF-5	550, 10	Inert	ZnO QD@C	LIBs	18
$[(HNTA)(H_2O)_3Zn]\cdot H_2O$	600, —	—	Microparticle of ZnO	Solar cells	20
$[(H_2O)_6Zn][(NTA)_2Zn_2]\cdot 2H_2O$	500, —	—	Microwires of ZnO	Solar cells	20
ZnMn6–PTCDA MMOFs	450, 5	Air	Spinel $ZnMn_2O_4$ nanoplates	LIBs	47
$[Mg_4(adipate)_4(DMA)\cdot(H_2O)]\cdot 5DMA\cdot 2MeOH\cdot 4H_2O$	500, 5	N_2	Nanoporous MgO	—	67
$Cu_3(BTC)_2$	500, —	—	Microplates of CuO	—	10
$Cu_3(BTC)_2$	500, 10	—	Coralloid Cu	—	16
$Cu_3(BTC)_2$	400, 10	—	Spongy CuO	—	13
$Cu_3(BTC)_2$	600, —	Air	CuO/CeO_2	CO oxidation	46
HKUST-1	400	Air	CuO–Ce_2O nanoparticles	CO oxidation	12
$[Cu_3(BTC)_2]_n$	550	Air	CuO	LIBs	68
$[Cu_3(BTC)_2]_n$	350		CuO/Cu_2O composite hollow polyhedrons	LIBs	17
$[Cu_3(BTC)_2]_n$	400, 5	N_2	Cu@C	Sensors	69
$[Cu_2(BDC–NH_2)_2(DABCO)]DMF\cdot 3H_2O$	500	Air	CuO	—	70
$[Cu_3(BTC)_2]_n$	300	N_2–air	Hollow octahedral CuO	LIBs	15
$[C_8H_{10}CdO_7]_n\cdot 4H_2O$	520, 5	Air	Nanowires of CdO	—	11
$Co_3(NDC)_3(DMF)_4$	600, 10	Air	Co_3O_4 nanoparticles	LIBs	35
CPP-3	550, —	—	Hexagonal rod-shaped In_2O_3	—	71
CPP-6	700, —	—	Hollow hexagonal In_2O_3	—	71
CPP-5	550, —	—	Hexagonal disk-shaped In_2O_3	—	71
Fe–EDTA	550, 10	—	Nanosheets of Fe_3O_4	—	14
PB	650, —	—	Hierarchical shell of Fe_2O_3	—	32
TiO_2 loading MIL-101	550	Air	Fe_2O_3 TiO_2 nanocomposite	Hydrogen production	72
MIL-10	600–800	N_2	N-doped graphene/Fe–Fe_3C nanocomposite	LIBs	73
MIL-53	600	N_2	Carbon–Fe_3O_4 nanocomposite	Superadsorbent material	58
$Fe_2(BDC)_3$	700	N_2	Nanorods of Fe_3O_4		33
MIL-88–Fe	500	N_2–air	Spindle-like mesoporous α-Fe_2O_3	LIBs	59
$[Al_8(OH)_{15}(H_2O)_3(BTC)_3]_n$	500/750	—	Cubic structured and coral structure dAl_2O_3 nanoparticles	—	74
Cd(NDC)(DMF)	600		CdO	—	75
$Cd_3(NDC)_4$	600		CdO	—	75
$Gd(H_2O)_3Co$	400/700/800	Air	$GdCoO_3$	Photocatalytic degradation of dyes	76
$Co_3[Co(CN)_6]_2$	550	Air	Co_3O_4 nanocages	LIBs	34
$Co_3[Co(CN)_6]_2$	400	Air	Co_3O_4 porous nanocages	LIBs	37
$[Co_3(ABTC)_3(BPY)_{1.5}(H_2O)_3]\cdot(H_2O)_2$	550, 4	Ar	Porous Co_3O_4	Supercapacitors	38
Co[Fe(CN)6]0.667	350	Air	Porous $CoFe_2O_4$	LIBs	77
CoMn–MOF	400	Air	$CoMn_2O_4$ spinel	—	78
NiMn–MOF	400	Air	$NiMn_2O_4$		79
In loading Co–BTC	700	Argon	$Co_3InC_{0.75}$	ORR	80
Al loading MIL-101	500/600/700/800/900	Air	Cr_2O_3/Al_2O_3	Isobutane dehydrogenation	81
Co loading MIL-100–Fe	700	Air	$CoFe_2O_4$	Phenol degradation	82

[a] TDA = $S(CH_2COO)_2$; CPP = coordination polymer particles; CPP-3 = $In_2(bdc)_3$; CPP-6 = In[2,6-bis[(4-carboxyanilino)carbonyl]pyridine]$_x$; PB = Prussian blue; NDC = 2,6-naphthalene-dicarboxylate; DMF = *N*,*N*-dimethylformamide; MIL-101 = $Fe_3(H_2O)_2(BDC)_3$ acid.

The TEM images of the Co/Co_3O_4 nanoparticles formed after thermolysis of three-dimensional $Co_6(BTC)_2(HCOO)_6(DMF)_6$ showed that the particle size was 40 nm, which is larger than the particle size of the Co/Co_3O_4 nanoparticles formed after thermolysis of $Co_2(hfbba)_2(3\text{-mepy})_2\cdot(DMF)_3$ (Co-HFMOF-D) (Fig. 6A–D). This result confirmed that the three-dimensional structure of the MOFs was responsible for particle growth during the reaction.

Compared with other transition metal MOFs, the Zn(II) ions or clusters in the Zn–MOFs were more resistant to

 This journal is © The Royal Society of Chemistry 2015

Published on 12 December 2014. Downloaded by Changchun Institute of Optics, Fine Mechanics and Physics, CAS on 29/05/2016 14:28:41.

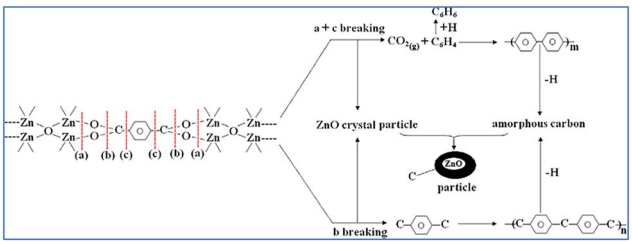

Fig. 3 Schematic illustration of the mechanism of decomposition of MOF-5. Reproduced with permission from Y. H. Hu *et al.*,[19] *J. Phys. Chem. C*, 2010, **114**. Copyright American Chemical Society (2010).

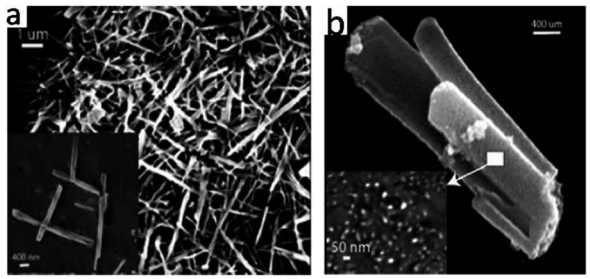

Fig. 4 (a) SEM micrographs of ZnO microwires. (b) SEM micrographs of ZnO nanoparticles. Reproduced with permission from H. Thakuria *et al.*,[20] *Eur. J. Inorg. Chem.*, 2007, **2007**. Copyright Wiley-VCH Verlag 524 GmbH & Co. KGaA, Weinheim (2007).

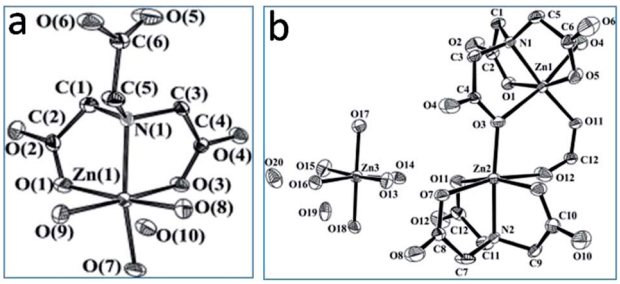

Fig. 5 Molecular structure of (a) the Zn–NTA complex with a metal to ligand ratio of 1 : 1. (b) Zn–NTA complex synthesized with a metal to ligand ratio of 3 : 2. Reproduced with permission from H. Thakuria *et al.*,[20] *Eur. J. Inorg. Chem.*, 2007, **2007**. Copyright Wiley-VCH Verlag 524 GmbH & Co. KGaA, Weinheim (2007).

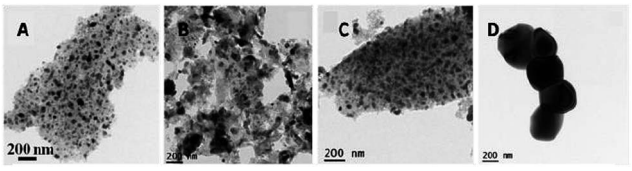

Fig. 6 (A and B) TEM images of Co nanoparticles prepared by thermolysis of (A) Co–HFMOF-D and (B) Co–BTC in nitrogen. (C,D) TEM images of Co_3O_4 nanoparticles prepared by thermolysis of (C) Co–HFMOF-D and (D) Co–BTC in air. Reproduced with permission from R. Das *et al.*,[31] *Nanoscale*, 2012, **4**. Copyright The Royal Society of Chemistry (2012).

agglomeration. In addition, the boiling point of Zn was lower. As a result of these properties, Zn–MOFs have recently attracted attention in the formation of porous carbon, *e.g.* Xu *et al.*[26] More detailed information has been published elsewhere.[27–30]

2.3 Fe_2O_3/Fe_3O_4

Iron oxide particles have been explored as a result of their wide range of functional applications. For example, hematite is used in diverse applications, including catalysis, LIBs and sensors. Magnetite has unique magnetic, optical, electronic and catalytic properties. Its versatility is largely determined by its morphology and structure; however, conventional methods, including hydrothermal synthesis, sol–gel synthesis, the use of templates and thermal decomposition have resulted in only limited success in finding relatively simple ways to produce iron oxide particles with a tunable size and specific shapes and structures.

Based on crystallography and growth mechanisms, MOFs have been used as templates for the synthesis of iron oxide particles *via* solid-state thermal decomposition. Many interesting iron oxide materials with the desired properties have now been reported.

Fe_2O_3 microboxes with hierarchically structured shells have been synthesized simply by annealing microcubes of Prussian blue (PB).[32] Based on the results of TGA, which showed that PB undergoes considerable weight loss at about 320 °C, the first transformation was performed at 350 °C. In this step, PB was transformed into a relatively smooth and dense iron oxide shell in the near-surface region. Continuous decomposition was completed at 550 °C with an outward gas flow, resulting in the formation of highly porous microboxes from enlarged Fe_2O_3 particles. Further increasing the annealing temperature to 650 °C transformed the highly porous shell into a well-defined, hierarchically structured shell consisting of Fe_2O_3 nanoplatelets. Fig. 7 shows products with distinct morphologies and structures that were obtained at different temperatures. This indicates that, with controlled procedures, aesthetically interesting micro/nanostructures can be harvested and their performances enhanced.

Chen *et al.*[14] synthesized single-crystal Fe_3O_4 nanosheets with an average edge length in the range 80–100 nm and a thickness of about 30 nm *via* the direct pyrolysis of an EDTA iron(III) salt at 350 °C in a horizontal tube furnace closed at one end. They investigated how the Fe^{3+} changed into Fe^{2+} without

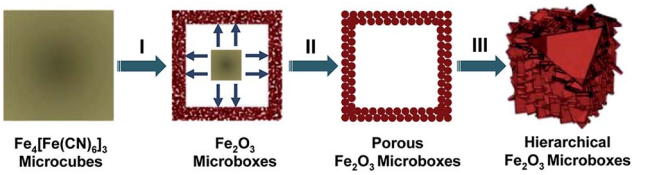

Fig. 7 Schematic illustration of the formation of hollow Fe_2O_3 microboxes and the evolution of the shell structure with increasing calcination temperature. Reproduced with permission from X. W. Lou *et al.*,[32] *J. Am. Chem. Soc.*, 2012, **134**. Copyright American Chemical Society (2012).

Published on 12 December 2014. Downloaded by Changchun Institute of Optics, Fine Mechanics and Physics, CAS on 29/05/2016 14:28:41.

any additional reductant at this low temperature. It was proposed that, with increasing temperature, the EDTA ferric sodium salt began to decompose thermally and the organic parts of the molecule decomposed into carbon and gases such as hydrogen and carbon monoxide, together with other fragments from the incompletely decomposed molecule. Reduction by this carbon and the decomposed gases converted some of the Fe^{3+} into Fe^{2+}. Fe_3O_4 was finally formed in the reducing atmosphere.

Cho *et al.*[33] developed a method to convert an Fe–MOF to hematite and then to magnetite. 1,4-Benzenedicarboxylate (BDC) and Fe^{3+} were used to form Fe–MIL-88B, a coordination polymer. Calcination of Fe–MIL-88B at 380 °C in air using a conventional furnace resulted in the formation of Fe_2O_3 nanorods. When the calcination conditions were slightly modified, magnetite was produced from the Fe–MIL-88B instead of hematite. The pyrolysis temperature was reduced to 300 °C to obtain hematite with incompletely calcined organic residues; this was confirmed by TGA and powder XRD. Cho *et al.*[33] suggested that the organic residues within the particles may act to reduce Fe(III) to Fe(II). The second thermal treatment, the calcination of hematite containing organic residues at up to 700 °C under a nitrogen atmosphere, resulted in pure magnetite nanoparticles. To investigate the role of the organic residues during the conversion process, several comparative experiments were performed. It was found that the rate of transformation of hematite into magnetite was related to the amount of organic residue and therefore to the holding time and temperature during the first thermal treatment. Based on these observations, the role of the organic residues generated in the incomplete first calcination as reducing reagents was confirmed.

The synthesis of Fe_3O_4 by a solid template method avoids harsh aqueous chemistry. In the transformation process, the residue and the atmosphere generated from the decomposition of the ligand both played a part in the reduction. This idea can be applied to other systems for producing metal compounds with a low valence state or the elemental metal.

2.4 Co/Co_3O_4

Another important MOF-derived nanostructured metal oxide is Co_3O_4, which has been considered as a potential material for use in LIBs since 2000 as a result of its high theoretical capacity as an electrode material. As a result of its enhanced capacity retention on cycling, various structures and textures of Co_3O_4 have attracted much attention, as have Co–MOFs. Xu *et al.*[35] successfully converted cobalt oxide subunits in a Co–MOF into agglomerated Co_3O_4 nanoparticles. MOF-derived Co_3O_4 was widely studied in subsequent years.[34–36] The Kirkendall effect has been used to explain the fabrication process for Co_3O_4 porous nanocages[37] using MOFs as a template in a similar manner to other MOF-derived hollow or shell structures, such as the Fe_3O_4 hierarchically structured shells and CuO hollow octahedral structures mentioned previously. Hu *et al.*[37] used a specific method involving dropwise addition through a syringe, low concentrations of reactants and PVP to obtain the uniform nanosized precursor $Co_3[Co(CN)_6]_2 \cdot nH_2O$. The solid particles were converted into Co_3O_4 porous nanocages at 400 °C in air after 1 h. During the thermal decomposition process, inter-diffusion led to the formation of cavities and the release of CO_2/N_xO_y gases generated from CN^- contributed to the porosity. The morphology and microstructure of the Co_3O_4 nanocages were determined by TEM and HRTEM (Fig. 8). As the temperature increased, the inter-diffusion of $Co_3[Co(CN)_6]_2$ and CO_2/N_xO_y increased and the porous cages collapsed. Similar to the synthesis of $Co_3[Co(CN)_6]_2 \cdot nH_2O$, the Prussian blue analogues (PBA) $M_3^{II}[M^{III}(CN)_6]_2 \cdot nH_2O$ (M = Mn, Fe, Co, Ni, Cu and Zn) could transform into metal oxides and even bimetal oxides. The controllable synthesis of PBA with different shapes and sizes has promoted the development of PBA-derived metal oxides because the performance of the metal oxides is closely related to the size, morphology and surface area.

The specific solid-state thermal conversion of Co–MOF into Co_3O_4 using $Co_3(ABTC)_3(BPY)_{1.5}(H_2O)_3$ as the precursor instead of PBA was reported by Meng *et al.*[38] After annealing under Ar at 550 °C for 1 h, the black powder was placed in a furnace at 400 °C for 1 h to remove the carbon residue generated from the organic linkers. The as-synthesized porous Co_3O_4 particles had a high specific capacitance of 150 F g^{-1} at a current density of 1 A g^{-1} and retained a slightly enhanced capacitance after 3400 cycles. This could be ascribed to its higher specific surface area and accessible channel structural features.

After publishing their work on the synthesis of hollow M/MONs, Zheng *et al.*[39] obtained hollow Co_3O_4 dodecahedrons with controllable interiors by one- or two-step pyrolysis. Fig. 9 shows that, at the initial stage of calcination, a Co_3O_4 dodecahedral shell was formed on the surface of the ZIF-67 [Co(2-methylimidazole)] core during the one-step method under an air atmosphere. Two forces with opposite directions acted on the interface between the Co_3O_4 shell and the ZIF-67 core as the calcination continued. The contraction force (F_c) associated with the formation of the Co_3O_4 crystallites led to the inward contraction of the Co_3O_4 core, whereas the adhesive force (F_a), resulting from the release of gases, prevented the inward contraction of the outer shell of Co_3O_4. For the two-step calcination method, the amorphous carbon generated from the organic ligands of ZIF-67 in the first calcination step served as a temporary framework to distribute the Co or CoO_x particles. During the second-step calcination under an air atmosphere, the outward force induced by the release of gases from the oxidization of carbon led to the outward diffusion of Co or CoO_x particles, which were simultaneously oxidized to Co_3O_4 by the air.

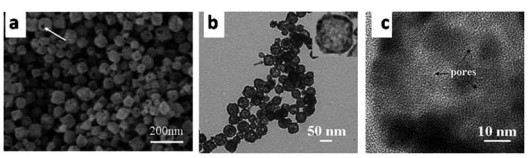

Fig. 8 (a) SEM image of the Co_3O_4 nanocages. (b,c) TEM images of Co_3O_4 porous nanocages at different magnifications. Reproduced with permission from Hu *et al.*,[37] *Chem. Eur. J.*, 2012, **18**. Copyright Wiley-VCH Verlag GmbH & Co. KGaA, Weinheim (2012).

 This journal is © The Royal Society of Chemistry 2015

Published on 12 December 2014. Downloaded by Changchun Institute of Optics, Fine Mechanics and Physics, CAS on 29/05/2016 14:28:41.

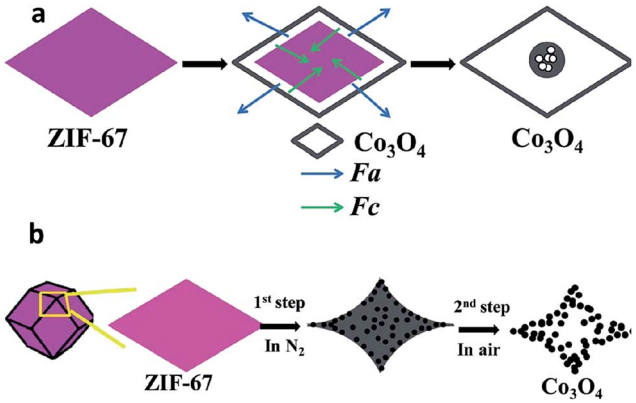

Fig. 9 (a) Schematic illustration of the formation of ball-in-dodecahedron Co_3O_4 by one-step calcination. (b) Schematic illustration of the formation of Co_3O_4 dodecahedrons with concave surfaces by two-step calcination. Reproduced with permission from Zheng *et al.*,[39] *J. Mater. Chem. A*, 2014, **2**. Copyright The Royal Society of Chemistry (2014).

It is important to investigate the conditions and mechanisms of decomposition when synthesizing the desired materials. The pore and void volumes of particles can be controlled by gas flow-rates as well as temperature. The challenge in calcination is the contraction of MOFs, which leads to crystal aggregation. Some methods using mild conditions have therefore been reported. An immersion method was used to construct $Co(OH)_2$ with [Co(BDC)(DMF)] as the precursor.[40] Co–NTCDA (NTCDA = 1,4,5,8-naphthalenetetracarboxylic dianhydride) or Co–PTCDA (PTCDA = perylene-3,4,9,10-tetracarboxylic dianhydride) was treated with an organic amine solution to form hydroxides *via* the hydrolysis of MOFs[41] (Fig. 10). An aqueous solution of TMAOH (25 wt%) or TPAOH (25 wt%) was added to a solution of Co–MOFs (Co–NTCDA or Co–PTCDA) in a cold bath at 10 °C with stirring to obtain CoO(OH) powders, which were then calcined in a furnace at 500 °C for 1 h at a heating rate of 1 °C min^{-1}. The final morphology of the metal oxides did not depend on the initial morphology of the MOF precursors. This result is different from previous reports of the preparation of metal oxides *via* the calcination of MOFs. The factors influencing the morphology of the metal oxides may involve the type of organic linker, the metal ion and the organic amine used.

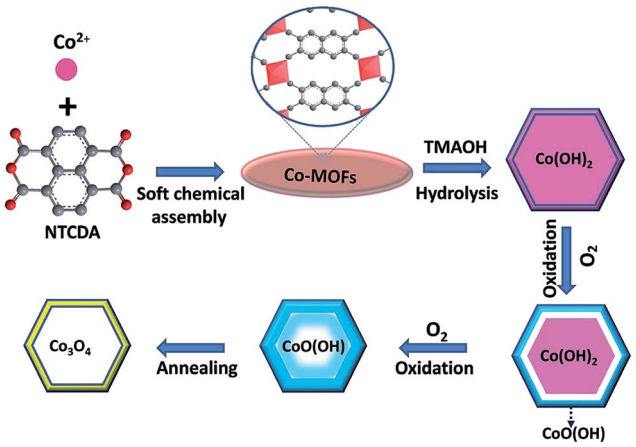

Fig. 10 Schematic illustration of the fabrication of Co_3O_4 hexagonal rings from Co-based MOFs. Reproduced with permission from Yang *et al.*,[41] *J. Mater. Chem. A*, 2014, **2**. Copyright The Royal Society of Chemistry (2014).

2.5 Bimetal oxides

The porous structure of MOFs is effective in dispersing metal ions. However, the metal ions or clusters of metal ions occupying the nodal positions in a crystalline framework are already well dispersed. Many metal-doped MOFs and metal@MOFs (MOFs loaded with metal ions), such as Cu, Ru, Pd, Au, Ag and Pt@ MOFs, have been reported.[42–45] The metal-doped MOFs and metal@MOFs can yield neat bimetal oxide composites when the metal ions are simultaneously converted into metal oxides.

For example, impregnating HKUST-1 with a 1 M ethanolic solution of Ce(III) nitrate hexahidrate before heat treatment allows the synthesis of a mixture of CuO and CeO_2 nanoparticles in intimate contact. This CuO/CeO_2 composite has a high catalytic activity for the oxidation of CO.[12,46]

A series of MMn_2O_4 (M = Ni, Zn, Co) particles with a spinel structure by the pyrolysis of mixed-MOF (MMOFs) precursors in air at 450 °C has been reported.[47] MMOFs consisting of two metal cations were synthesized using the corresponding metal acetates and PTCDA (PTCDA = perylene-3,4,9,10-tetracarboxylic dianhydride) as a ligand. The mixed transition metal oxide materials showed a high initial capacity of 1100 mA h g^{-1} and a retained capacity of 600 mA h g^{-1} after 20 cycles.

An etching method has been used to synthesize hollow MMONs by Zhang *et al.*[48] NaOH was used as an etching agent and the reaction between PB microcubes and the NaOH solution led to the formation of $Fe(OH)_3$ microboxes with a controllable multishelled structure. In addition, the PB microcubes reacted with the conjugated bases of weak acids based on metal oxides, generating multicompositional microboxes (Fe_2O_3/SnO_2, Fe_2O_3/SiO_2, Fe_2O_3/GeO_2, Fe_2O_3/Al_2O_3 and Fe_2O_3/B_2O_3). These consisted of uniformly dispersed oxides/hydroxides of Fe and another designed element (Fig. 11). Fe_2O_3/MO_x were then obtained by annealing the cubes. The as-formed Fe_2O_3/MO_x was etched by HCl with the preservation of the MO_x configuration.[48] The $MO_x \cdot nH_2O$ should be a weak acid so that the Fe(III) can simultaneously react with the conjugate bases during hydrolysis; the weakly acidic $MO_x \cdot nH_2O$ is not etched by HCl. These hollow cubes and atomically integrated multiple compositions have the usual physiochemical properties.

2.6 Metal/metal oxide–carbon composite

The organic framework decomposes into gaseous products (CO_2, NO_x and hydrocarbons) and carbon when there is a lack of oxygen, so the pyrolysis of MOFs always yields carbon-coated metal oxides; this method has been reported since 2008.[26,49–57] MOF-derived carbon has attracted much attention as a result of its porosity, high surface area, hierarchical structure and use as

Published on 12 December 2014. Downloaded by Changchun Institute of Optics, Fine Mechanics and Physics, CAS on 29/05/2016 14:28:41.

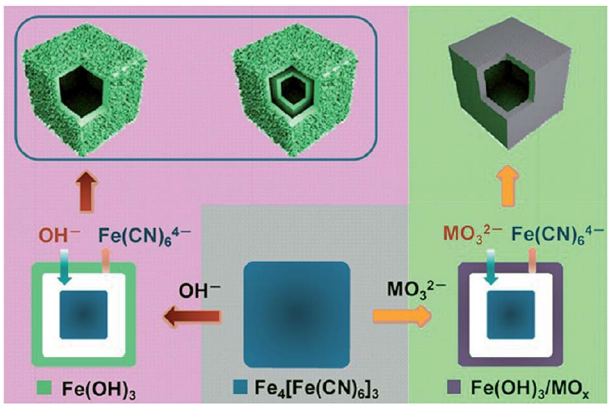

Fig. 11 Schematic illustration of the formation of hierarchical (left) and multicompositional (right) metal oxide microboxes starting with MOF templates. The metal oxides microboxes were synthesized by manipulating the ion-exchange reaction between an alkaline precursor (strong base or conjugate base of the weak acid) and sacrificial PB. Reproduced with permission from Zhang *et al.*,[48] *J. Am. Chem. Soc.*, 2013, **135**. Copyright American Chemical Society (2013).

an sorbent for gases or liquids, as a catalyst support, electrode material and in fuel cells as carbon-coated oxides.[18,58] A carbon composite with Fe_3O_4 nanoparticles was synthesized by the pyrolysis of Fe-containing MOFs at different temperatures in an argon atmosphere.[58] Cu/CuO, Co/Co_3O_4, ZnO, Mn_2O_3, MgO and CdS/CdO embedded in a carbon matrix have also been synthesized through the controlled thermolysis of MOFs. MOF-5 has been used as a sample to systematically investigate the changes in the carbon during the thermal process.[19] MOF-5 was heated to 480 °C at a heating rate of 10 °C min^{-1} in a vacuum and 40.5% of the weight was lost. The remaining 59.5 wt% consisted of ZnO powder and carbon as determined by elemental analysis and XRD. The Raman spectrum of the decomposed MOF-5 showed the same bands located at 325, 328, and 433 cm^{-1} as in commercial ZnO powder. After removing the ZnO by washing with hydrochloric acid, the characteristics of amorphous carbon were observed in the XRD pattern and the Raman spectrum. The bands at 1320 and 1592 cm^{-1} were the same as those observed for amorphous carbon. With heat treatment in flowing air, the carbon was oxidized to CO_2.[15,59] After further heating at 900 °C in air for 3 h, the Raman spectrum of the sample was almost the same as that of commercial ZnO as a result of the removal of carbon from the decomposed MOF-5.

Carbon doped with transition metals and nitrogen (TM/N/C) has been used in electrocatalysts for the oxygen reduction reaction (ORR) in fuel cells. Liu and co-workers[60,61] pyrolyzed Co–ZIF and Fe–ZIF to produce Co–N–C and Fe–N–C, respectively. Increasing the pyrolysis temperature was detrimental as a result of the loss of N and a decrease in the specific surface area. To circumvent these shortcomings, Fe–ZIF was mixed with ZIF-8, which provided both a high N content and a high specific surface area. ZIF-8 dilutes the Fe content and disturbs the crystallization of carbon, making graphitization difficult as a result of the evaporation of Zn. ZIF-8 produces the pyrolyzed product at even higher temperatures and retains the amorphous carbon structure. As a result of this amorphous structure, FeIM/ZIF-8 has a better mass transport property and a higher N content brought about by the facile reaction with NH_3. Research focused on the use of bimetal ZIF to synthesize N-doped nanotubes has been reported.[62,63] The conversion benefitted from the use of materials containing Fe as the catalytic sites for graphitization and Zn to form pores.

The design of MOF precursors, such as controlling their shape or size and changing the ratio of the ligand C and N atoms to the transition metal may increase the performance of the derived materials. This is worth exploring and the mature methodologies for the synthesis of MOFs have made it possible. As an example, MOFs grown on Cu foil were designed to prepare hybrid porous nanowire arrays composed of strongly interacting Co_3O_4 and carbon by a facile carbonization method.[64] The resulting material was used as the working electrode in an oxygen evolution reaction. In another study, ZIF-8 coated with organic molecules (*e.g.* hydroxyl, pyrrolyl and/or carboxyl functionalized organic molecules) was decomposed at 800 °C to prepare metal oxide–carbon nanocomposites.[65] The uniformly distributed ZnO in the carbon is beneficial for storing more lithium ions in the anodes and thus leads to high specific capacities and better retention.

We have drawn the following conclusions: (1) calcination of the relevant template is an important method for the transformation of MOFs into metal oxides; (2) the temperature, time and atmosphere are key factors in thermal decomposition, and can be guided by the TGA curve – in general, larger crystals are formed at higher temperatures, carbon-coated metal oxides are formed in inert gas and pure metal oxide are formed in air; (3) the gas generated from the decomposition of the organic ligand and crystal growth both lead to the development of porosity, although inter-diffusion may lead to hollow structures; (4) the spatial structure of MOFs affects the size and morphology of the as-synthesized metal/metal oxides; and (5) metal ions with a reduction potential of −0.27 V or higher in MOFs always form metal nanoparticles during thermolysis in N_2, whereas metal ions with a reduction potential less than −0.27 V form metal oxide nanoparticles during thermolysis in N_2 (Fig. 12). Table 1 summarizes all the reported MMONs and their possible applications.

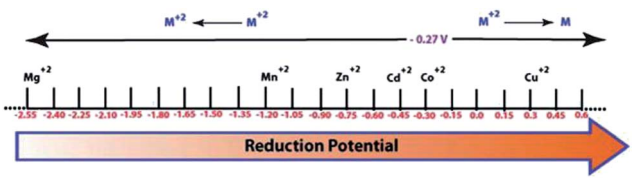

Fig. 12 Effect of the reduction potential of metal atoms present in MOFs on the formation of metal/metal oxide nanoparticles. Metals with a reduction potential higher than −0.27 V undergo thermolysis in an N_2 atmosphere to give pure metal nanoparticles, whereas metals with reduction potential less than −0.27 V, even in an N_2 atmosphere, produce metal oxides only. Reproduced with permission from Das *et al.*,[31] *Nanoscale*, 2012, **4**. Copyright The Royal Society of Chemistry (2012).

 This journal is © The Royal Society of Chemistry 2015

Published on 12 December 2014. Downloaded by Changchun Institute of Optics, Fine Mechanics and Physics, CAS on 29/05/2016 14:28:41.

3. Applications

As the performance of metal/metal oxides depends strongly on their morphology and size, MOF-derived micro/nanostructures with defined morphologies show many unique properties, *e.g.* a high photocatalytic activity, a high adsorption capacity, good electrocatalytic activity and outstanding electrochemical performance. These properties have led to applications in many fields, such as LIBs,[15,17,18,32,34,35,37,59,83–85] electrochemical capacitors,[21,38] sensors, in catalysis[12,36,46,72,81,82] and in gas absorption/separation.[58]

3.1 Electrode materials for batteries

The poor electron-conducting properties of most MOFs excludes them from electrochemical applications. However, several methods, such as isomorphous replacement,[86] introducing MOFs directly as counter ions[87] and loading MOFs on conductive materials,[88] have been applied to improve their proton/electron conductivity properties. The most common and practical method is to use MOFs as sacrificial precursors in the formation of transition metal oxide nanoparticles, which are often used as electrochemical materials. Agglomerated Co_3O_4 nanoparticles derived from Co–MOFs have been used successfully in LIBs.[11] Fig. 13a shows the charge/discharge curves of as-prepared Co_3O_4 in an Li^+ test cell at a current density of 50 mA g^{-1}. A high discharge capacity (1118 mA h g^{-1}) was produced during the first discharge process. The initial capacity retention is up to 75% in the first cycle. The capacity shows a gradual increase in subsequent cycles to a peak value of 965 mA h g^{-1} at the 50th cycle (Fig. 13b), which is 86% of the initial capacity. This may be attributed to the unique structural characteristic of the agglomerated Co_3O_4. The cycle performance at a higher current density of 100 mA shows a similar behavior to that measured at a current density of 50 mA g^{-1} (Fig. 12c and d). The capacity in the first discharge cycle is 1090 mA h g^{-1}, 730 mA h g^{-1} of which remains beyond 100 cycles with a highest value of 824 mA h g^{-1} at the 39th cycle (Fig. 13d). In spite of the agglomerate structure and low surface area of the Co_3O_4, its capacity for Li storage compares favorably with non-agglomerated cobalt oxide nanostructures.[89] It is clear that the agglomerated Co_3O_4 nanocrystalline particles have a superior electrochemical performance as electrode materials for LIBs as a result of their unique primary/secondary agglomerated structure.

Carbon-coated ZnO showed promising Li storage properties and a high specific charge capacity (about 1200 mA h g^{-1} at 75 mA g^{-1}).[18] The capacity was estimated on the basis of the total composite weight, the stable cycling ability (about 50 cycles with nearly 100% capacity retention) and the good performance rate (about 400 mA h g^{-1} at 3750 mA g^{-1}). A number of metal oxides, such as Fe_2O_3 microboxes with hierarchical shell structures and porous CuO hollow octahedral mesoporous $ZnCo_2O_4$ microspheres synthesized from MOFs, have been used in LIBs and the corresponding data are given in Table 1.

Sulfur-loaded MOF-derived carbon was used to fabricate cathode structures for lithium–sulfur batteries by Xi *et al.*[54] Four types of Zn-containing MOFs were carbonized to give unique carbon materials with different hierarchical pore structures. A thermal process was used to load the pyrolyzed carbon with sulfur and 55 wt% sulfur was incorporated into the porous carbon host matrix. The $[Zn_3(fumarate)_3(DMF)_2]$-derived cathode materials produced higher mesopore (2–50 nm) volumes that showed increased initial discharge capacities, whereas the carbons with higher micropore (<2 nm) volumes made from ZIF-8 led to cathode materials with better cycle stability.

3.2 Electrode materials for supercapacitors

The special surface texture and morphology of Co_3O_4 nanoparticles obtained by simple thermolysis of Co–MOF crystals *via* a two-step calcination treatment was used in a supercapacitor electrode.[38] The storage performance tested in KOH solvent showed that the porous Co_3O_4 particles had a high specific capacitance of 150 F g^{-1} at a current density of 1 A g^{-1}. As a result of their high specific surface area and accessible channel structural features, the well-defined Co_3O_4 particles retained slightly enhanced capacitance after 3400 cycles.

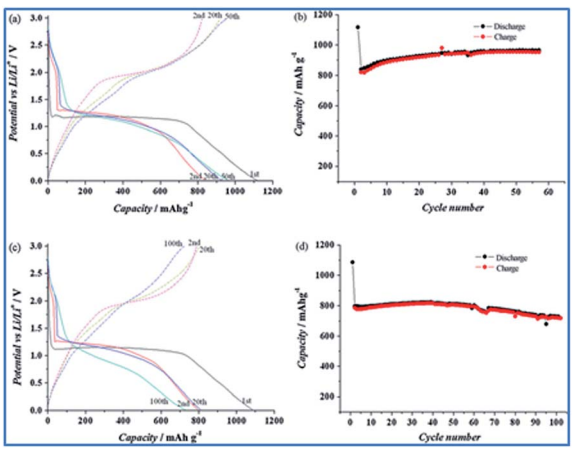

Fig. 13 (a) Charge–discharge curves and (b) cycle performance at a current density of 50 mA g^{-1} and (c) charge–discharge curves and (d) cycle performance at a current density of 100 mA g^{-1} for the as-prepared Co_3O_4/Li half-cell cycled between 3.0 and 0.01 V. Only the mass of Co_3O_4 was considered in calculating the specific capacity. Reproduced with permission from Liu *et al.*,[35] *J. Power Sources*, 2010, **195**. Copyright Elsevier B.V. (2009).

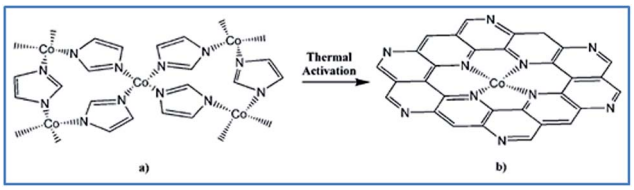

Fig. 14 Proposed structural conversion from Co–ZIF to the active catalytic site. Reproduced with permission from D. J. Liu *et al.*,[60] *Chem.–Eur. J.*, 2011, **17**. Copyright Wiley-VCH Verlag GmbH & Co. KGaA, Weinheim (2011).

Published on 12 December 2014. Downloaded by Changchun Institute of Optics, Fine Mechanics and Physics, CAS on 29/05/2016 14:28:41.

In spite of their advantages of controllable shapes and structures, it is difficult to find examples where the use of MOFs as electrode materials resulted in a clear advantage in performance and durability. For real breakthroughs, MOFs will probably need to be designed and optimized with respect to their ionic and electronic conductivities.

3.3 Homogeneous catalysts

$CoFe_2O_4$ has been synthesized using a MOF template and precursors.[82] $Co(NO_2)_2 \cdot 6H_2O$ dispersed in ethanol was dropped into MIL-100–Fe prepared according to the method reported by Horcajada *et al.*[90] at a Fe/Co molar ratio of 1 : 1 or 1 : 2. The mixed ethanol solution was evaporated at 80 °C for 4 h. The obtained solid was then heat-treated at different temperatures (400, 500, 600 and 700 °C) for 4 h. The cobalt nitrate hexahydrate used as a second precursor was immobilized in the pores of the MOFs by incipient wetness impregnation. The as-synthesized $CoFe_2O_4$ nanocomposite particles retained the morphology of the template. Using potassium peroxymonosulfate as an oxidant, the magnetic nanomaterials showed a relatively high catalytic performance for the oxidation degradation of phenol. After 120 min of degradation, the phenol concentration was reduced by approximately 95%. The regenerated catalysts showed a high catalytic performance in consecutive runs, except for the product obtained from precursors at a Fe/Co molar ratio of 1 : 2 at 700 °C. It was suggested that Fe(III) promoted the regeneration of the Co(II)–OH complexes, which is the rate-limiting step for Co(II)-mediated PMS activation process; Co_3O_4 has been demonstrated to be inferior in this process. However, MIL100–Fe 1:2–700 was composed of Co_3O_4 and $CoFe_2O_4$, with no Fe(III).

Isobutene dehydrogenation over mesoporous Cr_2O_3/Al_2O_3 catalysts synthesized from the MOF MIL-101 has been reported.[81] The catalytic activity and selectivity were related to the Cr^{3+}/Cr^{6+} ratio. The template method facilitates the control of the Cr^{3+}/Cr^{6+} volume during the catalysis. A series of non-ordered mesoporous chromia/alumina catalysts with large specific surface areas (149.4–381.6 $m^2\ g^{-1}$) and high pore volumes (0.77–1.24 $cm^3\ g^{-1}$) was synthesized. With increasing chromia loadings (5–25 wt%) and calcination temperatures (500–900 °C), the specific surface area of the catalyst decreased, whereas the amount of surface Cr^{3+} species and the molar ratio of the Cr^{3+} and Cr^{6+} species (Cr^{3+}/Cr^{6+}) increased. The catalyst with 10 wt% Cr_2O_3 loading calcined at 800 °C showed the highest isobutene conversion 60.1%, with an isobutene selectivity of up to 93.2%. The addition of potassium to the catalyst system promoted the selectivity toward isobutene and the catalyst stability. The catalyst with 1.5 wt% K_2O showed an ideal performance. The catalytic reactivity showed high stability over ten dehydrogenation–regeneration cycles.

Other catalytic nanomaterials such as $CuO–CeO_2$ nanoparticle catalysts for CO oxidation,[46] $GdCoO_3$ for the photocatalytic degradation of dyes[76] and $Fe_2O_3–TiO_2$ nanocomposites for hydrogen production[72] are listed in Table 1.

3.4 Oxygen reduction reaction

The catalytic ORR at the cathode is a critical process in the operation of proton-exchange membrane fuel cells. The cathode in the ORR is six or more orders of magnitude slower than the anode and thus limits the performance of fuel cells; there is an urgent need to develop suitable catalysts for the ORR. The current cathode catalyst materials of choice are the platinum group metals (PGMs), but these are expensive, have a low tolerance to methanol and limited stability. However, R. Jasinski have reported ORR activity for a Co–polypyrrole composite, which was attributed to Co ligated by pyrrolic nitrogen at the catalytic site. Inspired by the ORR catalytic activity of cobalt phthalocyanine, the search for non-PGM electrocatalysts is mainly focused on TM/N/C composites. A significant enhancement in ORR activity has been demonstrated in C-supported Fe-based catalysts and it was suggested that micropores (width <2 nm) have a critical influence on the formation of the active site, which has a structure of cationic ions coordinated by four pyridinic nitrogens.[92]

Co–ZIF has been reported to be a precursor for a TM/N/C nanomaterial with a uniformly distributed catalytic center and a highly active site for the ORR. During thermal activation, the C and N in the imidazolate ligand become the active site, as evidenced by X-ray photoelectron spectroscopy before and after heat treatment. It was found that C remained mainly as the original organic moiety at 500 °C and was converted to carbonaceous (at 750 °C) and graphitic (at 900 °C) forms with increasing activation temperature. N maintained the imidazolate form at 500 °C. After activation at 750 °C, X-ray photoelectron spectroscopy showed that N was converted to a mixture of pyridinic- and pyrrolic-like moieties, with the former the dominant component (Fig. 14). Fe–ZIF has also been used as a precursor to prepare electrocatalysts because Fe is more efficient than Co in TM/N/C catalysts.[61,93] A common difficulty is that, although high temperatures favor the transformation of the precursor into an active site, this is detrimental as a result of the loss of N and a decrease in the specific surface area. To overcome this limitation, the mixing in of additional N, the addition of C and enhancement of the ratio of porosity have been investigated. A typical example is the novel design of a bimetal ZIF.[94] Zn as the major component in this ZIF forms pores and suppresses graphitization, which decreases the specific surface area and mass transport property; Fe as the minor component forms the catalytic sites.

4. Conclusions and outlook

We have drawn the following conclusions.

(1) There has been an unprecedented rapid growth in the field of MOFs in the last decade. Although early studies focused mainly on the structural diversity and applications of MOFs, the research trend has now shifted toward different MOF-derived materials and their potential applications.

(2) The pyrolysis of MOFs has been a focal point in MOF studies since 2005.[95] Significant progress has been made in the

 This journal is © The Royal Society of Chemistry 2015

Published on 12 December 2014. Downloaded by Changchun Institute of Optics, Fine Mechanics and Physics, CAS on 29/05/2016 14:28:41.

synthesis of metal/metal oxides, metal oxide@C and porous carbon with various structures and compositions. Their applications are mainly in electrochemistry, including supercapacitors, batteries, fuel cells, sensing and catalysis. They may have other potential applications, such as in semiconductors or electronic devices.

(3) The main challenge in this field is determining the mechanism of conversion from the MOF to the derived materials. A transformation model should be developed to guide future investigations. A method to induce a controlled conversion with packing of the atoms on the surface or exposed facets of a nanocrystal would be of great interest.

(4) Other transformation methods are needed to replace the inadequate calcination and immersion techniques. In addition, the design of novel MOFs with different particles sizes and structures may be an effective way to improve the properties of the derived materials.

(5) Except for oxides, hydroxides and porous carbon, the MOF template method is a potential synthesis method. It has been used to obtain CuS by selecting $[CH_3(CH_2)_{18}COO]_2Cu$ as a molecular template.[96] More compounds may be synthesized using this method in the future.

In conclusion, research into MOF-derived nanostructures has made great progress in the last decade, although this is just the tip of the iceberg with respect to their potential applications and synthesis methods. Many new types of nanoparticles will emerge as research topics. The advantages of this environmentally friendly technology, the possibility of mass production and low costs may make this material promising for future industrial applications.

Abbreviations

IRZIF	Isoreticular zeolitic imidazolate framework
TDA	$S(CHCOO)_2^{2-}$
CPP	Coordination polymer particles
PB	Prussian blue
NDC	2,6-Naphthalene dicarboxylate
DMF	*N*,*N*-Dimethylformamide
BTC	Benzene-1,3,5-tricarboxylate
BDC	Benzenedicarboxyylate
NTA	Nitrilotriacetic
H_3ABTC	Azobenzene-3,5,4′-tricarboxylic acid
BPY	4,4′-Bipyridine
Mepy	3-Methyl-pyridine
H_2hfbba	4,4′-(Hexafluoroisopropylidene)bis(benzoic acid)
NTCDA	1,4,5,8-Naphthalenetetracarboxylic dianhydride
PTCDA	Perylene-3,4,9,10-tetracarboxylic dianhydride
ZTC	Zeolite-templated carbon
ORR	Oxygen reduction reaction
MCNTs	Multiwalled carbon nanotubes
TMAOH	Tetramethylammonium hydroxide
TPAOH	Tetrapropylammonium hydroxide

Acknowledgements

This work was financially supported by the National Natural Science Foundation of China (21165010, 21465014 and 21465015), the Natural Science Foundation of Jiangxi Province (20142BAB203101), the Young Scientist Foundation of Jiangxi Province (20122BCB23011), the Ministry of Education by the Specialized Research Fund for the Doctoral Program of Higher Education (20133604110002) and the Ground Plan of Science and Technology Projects of Jiangxi Educational Committee (KJLD14023).

Notes and references

1 A. Morozan and F. Jaouen, *Energy Environ. Sci.*, 2012, **5**, 9269.
2 J. R. Li, Y. Tao, Q. Yu, X. H. Bu, H. Sakamoto and S. Kitagawa, *Chem.–Eur. J.*, 2008, **14**, 2771–2776.
3 J. Lee, O. K. Farha, J. Roberts, K. A. Scheidt, S. T. Nguyen and J. T. Hupp, *Chem. Soc. Rev.*, 2009, **38**, 1450–1459.
4 R. J. Kuppler, D. J. Timmons, Q. R. Fang, J. R. Li, T. A. Makal, M. D. Young, D. Yuan, D. Zhao, W. Zhuang and H. C. Zhou, *Coordin. Chem.Rev.*, 2009, **253**, 3042–3066.
5 A. Dhakshinamoorthy and H. Garcia, *Chem. Soc. Rev.*, 2012, **41**, 5262–5284.
6 U. Mueller, M. Schubert, F. Teich, H. Puetter, K. Schierle-Arndt and J. Pastre, *J. Mater. Chem.*, 2006, **16**, 626–636.
7 S. L. James, *Chem. Soc. Rev.*, 2003, **32**, 276–288.
8 B. S. T. Meek, J. A. Greathouse and a. M. D. Allendorf, *Adv. Mater.*, 2011, **23**, 249–267.
9 J. Juan-Alcañiz, J. Gascon and F. Kapteijn, *J. Mater. Chem.*, 2012, **22**, 10102–10118.
10 H. Thakuria and G. Das, *Polyhedron*, 2007, **26**, 149–153.
11 F. Zhang, F. L. Bei, J. M. Cao and X. Wang, *J. Solid State Chem.*, 2008, **181**, 143–149.
12 J. M. Zamaro, N. C. Pérez, E. E. Miró, C. Casado, B. Seoane, C. Téllez and J. Coronas, *Chem. Eng. J.*, 2012, **195–196**, 180–187.
13 L. Chen, C. Zhao, Z. Wei, S. Wang and Y. Gu, *Mater. Lett.*, 2011, **65**, 446–449.
14 L. Chen, C. Zhao, Y. Zhou, H. Peng and Y. Zheng, *J. Alloys Compd.*, 2010, **504**, L46–L50.
15 R. Wu, X. Qian, F. Yu, H. Liu, K. Zhou, J. Wei and Y. Huang, *J. Mater. Chem. A*, 2013, **1**, 11126.
16 L. Chen, Y. Shen, J. Bai and C. Wang, *J. Solid State Chem.*, 2009, **182**, 2298–2306.
17 L. Hu, Y. Huang, F. Zhang and Q. Chen, *Nanoscale*, 2013, **5**, 4186–4190.
18 S. J. Yang, S. Nam, T. Kim, J. H. Im, H. Jung, J. H. Kang, S. Wi, B. Park and C. R. Park, *J. Am. Chem. Soc.*, 2013, **135**, 7394–7397.
19 L. Zhang and Y. H. Hu, *J. Phys. Chem. C*, 2010, **114**, 2566–2572.
20 H. Thakuria, B. M. Borah and G. Das, *Eur. J. Inorg. Chem.*, 2007, **2007**, 524–529.
21 S. J. Yang, J. H. Im, T. Kim, K. Lee and C. R. Park, *J. Hazard. Mater.*, 2011, **186**, 376–382.

Published on 12 December 2014. Downloaded by Changchun Institute of Optics, Fine Mechanics and Physics, CAS on 29/05/2016 14:28:41.

22 Y. Zhang, D. Lan, Y. Wang, H. Cao and H. Jiang, *Phys. E*, 2011, **43**, 1219–1223.
23 M. C. Wu and C. S. Lee, *Inorg. Chem.*, 2006, **45**, 9634–9636.
24 T. Kundu, S. C. Sahoo and R. Banerjee, *Cryst. Growth Des.*, 2012, **12**, 2572–2578.
25 S. Jung, W. Cho, H. J. Lee and M. Oh, *Angew. Chem.*, 2009, **48**, 1459–1462.
26 B. Liu, H. Shioyama, T. Akita and Q. Xu, *J. Am. Chem. Soc.*, 2008, **130**, 5390–5391.
27 P. Pachfule, B. P. Biswal and R. Banerjee, *Chem.–Eur. J.*, 2012, **18**, 11399–11408.
28 B. Liu, H. Shioyama, H. Jiang, X. Zhang and Q. Xu, *Carbon*, 2010, **48**, 456–463.
29 W. Chaikittisilp, M. Hu, H. Wang, H. S. Huang, T. Fujita, K. C. Wu, L. C. Chen, Y. Yamauchi and K. Ariga, *Chem. Commun.*, 2012, **48**, 7259–7261.
30 Y. Han, P. Qi, S. Li, X. Feng, J. Zhou, H. Li, S. Su, X. Li and B. Wang, *Chem. Commun.*, 2014, **50**, 8057–8060.
31 R. Das, P. Pachfule, R. Banerjee and P. Poddar, *Nanoscale*, 2012, **4**, 591–599.
32 L. Zhang, H. B. Wu, S. Madhavi, H. H. Hng and X. W. Lou, *J. Am. Chem. Soc.*, 2012, **134**, 17388–17391.
33 W. Cho, S. Park and M. Oh, *Chem. Commun.*, 2011, **47**, 4138–4140.
34 N. Yan, L. Hu, Y. Li, Y. Wang, H. Zhong, X. Hu, X. Kong and Q. Chen, *J. Phys. Chem. C*, 2012, **116**, 7227–7235.
35 B. Liu, X. Zhang, H. Shioyama, T. Mukai, T. Sakai and Q. Xu, *J. Power Sources*, 2010, **195**, 857–861.
36 W. Wang, Y. Li, R. Zhang, D. He, H. Liu and S. Liao, *Catal. Commun.*, 2011, **12**, 875–879.
37 L. Hu, N. Yan, Q. Chen, P. Zhang, H. Zhong, X. Zheng, Y. Li and X. Hu, *Chem.–Eur. J.*, 2012, **18**, 8971–8977.
38 F. Meng, Z. Fang, Z. Li, W. Xu, M. Wang, Y. Liu, J. Zhang, W. Wang, D. Zhao and X. Guo, *J. Mater. Chem. A*, 2013, **1**, 7235.
39 J. Shao, Z. Wan, H. Liu, H. Zheng, T. Gao, M. Shen, Q. Qu and H. Zheng, *J. Mater. Chem. A*, 2014, **2**, 12194–12200.
40 D. O. Miles, D. Jiang, A. D. Burrows, J. E. Halls and F. Marken, *Electrochem. Commun.*, 2013, **27**, 9–13.
41 P. Su, S. Liao, F. Rong, F. Wang, J. Chen, C. Li and Q. Yang, *J. Mater. Chem. A*, 2014, **2**, 17408–17414.
42 C. Wang, K. E. deKrafft and W. Lin, *J. Am. Chem. Soc.*, 2012, **134**, 7211–7214.
43 Y. Zhao, J. Zhang, J. Song, J. Li, J. Liu, T. Wu, P. Zhang and B. Han, *Green Chem.*, 2011, **13**, 2078.
44 T. Ishida, M. Nagaoka, T. Akita and M. Haruta, *Chem.–Eur. J.*, 2008, **14**, 8456–8460.
45 S. Hermes, M. K. Schroter, R. Schmid, L. Khodeir, M. Muhler, A. Tissler, R. W. Fischer and R. A. Fischer, *Angew. Chem.*, 2005, **44**, 6237–6241.
46 F. Zhang, C. Chen, W.-m. Xiao, L. Xu and N. Zhang, *Catal. Commun.*, 2012, **26**, 25–29.
47 J. Zhao, F. Wang, P. Su, M. Li, J. Chen, Q. Yang and C. Li, *J. Mater. Chem.*, 2012, **22**, 13328.
48 L. Zhang, H. B. Wu and X. W. Lou, *J. Am. Chem. Soc.*, 2013, **135**, 10664–10672.
49 L. Chen, J. Bai, C. Wang, Y. Pan, M. Scheer and X. You, *Chem. Commun.*, 2008, 1581–1583.
50 J. Hu, H. Wang, Q. Gao and H. Guo, *Carbon*, 2010, **48**, 3599–3606.
51 H. L. Jiang, B. Liu, Y. Q. Lan, K. Kuratani, T. Akita, H. Shioyama, F. Zong and Q. Xu, *J. Am. Chem. Soc.*, 2011, **133**, 11854–11857.
52 L. Radhakrishnan, J. Reboul, S. Furukawa, P. Srinivasu, S. Kitagawa and Y. Yamauchi, *Chem. Mater.*, 2011, **23**, 1225–1231.
53 N. L. Torad, M. Hu, Y. Kamachi, K. Takai, M. Imura, M. Naito and Y. Yamauchi, *Chem. Commun.*, 2013, **49**, 2521–2523.
54 K. Xi, S. Cao, X. Peng, C. Ducati, R. V. Kumar and A. K. Cheetham, *Chem. Commun.*, 2013, **49**, 2192–2194.
55 S. J. Yang, J. H. Im, H. Nishihara, H. Jung, K. Lee, T. Kyotani and C. R. Park, *J. Phys. Chem. C*, 2012, **116**, 10529–10540.
56 S. J. Yang, T. Kim, J. H. Im, Y. S. Kim, K. Lee, H. Jung and C. R. Park, *Chem. Mater.*, 2012, **24**, 464–470.
57 D. Yuan, J. Chen, S. Tan, N. Xia and Y. Liu, *Electrochem. Commun.*, 2009, **11**, 1191–1194.
58 A. Banerjee, R. Gokhale, S. Bhatnagar, J. Jog, M. Bhardwaj, B. Lefez, B. Hannoyer and S. Ogale, *J. Mater. Chem.*, 2012, **22**, 19694.
59 X. Xu, R. Cao, S. Jeong and J. Cho, *Nano Lett.*, 2012, **12**, 4988–4991.
60 S. Ma, G. A. Goenaga, A. V. Call and D. J. Liu, *Chem.–Eur. J.*, 2011, **17**, 2063–2067.
61 D. Zhao, J.-L. Shui, C. Chen, X. Chen, B. M. Reprogle, D. Wang and D.-J. Liu, *Chem. Sci.*, 2012, **3**, 3200.
62 K. N. Z. Zeng and V. A. Maroni, *Oxid. Met.*, 2002, **58**, 147–170.
63 A. Oya and H. Marsh, *J. Mater. Sci.*, 1982, **17**, 309–322.
64 T. Y. Ma, S. Dai, M. Jaronie and S. Z. Qiao, *J. Am. Chem. Soc.*, 2014, **136**, 14385–14388.
65 Y. Han, P. Qi, S. Li, X. Feng, J. Zhou, H. Li, S. Su, X. Lib and B. Wang, *Chem. Commun.*, 2014, **50**, 8057–8060.
66 L. Chen, H. Xing, Y. Shen, J. Bai and G. Jiang, *J. Solid State Chem.*, 2009, **182**, 1387–1395.
67 T. K. Kim, K. J. Lee, J. Y. Cheon, J. H. Lee, S. H. Joo and H. R. Moon, *J. Am. Chem. Soc.*, 2013, **135**, 8940–8946.
68 A. Banerjee, U. Singh, V. Aravindan, M. Srinivasan and S. Ogale, *Nano Energy*, 2013, **2**, 1158–1163.
69 H. Tan, C. Ma, L. Gao, Q. Li, Y. Song, F. Xu, T. Wang and L. Wang, *Chem.–Eur. J.*, 2014, **20**, 16377–16383.
70 M. A. Alavi, A. Morsali, S. W. Joo and B. K. Min, *Ultrason. Sonochem.*, 2015, **22**, 349–358.
71 W. Cho, Y. H. Lee, H. J. Lee and M. Oh, *Chem. Commun.*, 2009, 4756–4758.
72 K. E. deKrafft, C. Wang and W. Lin, *Adv. Mater.*, 2012, **24**, 2014–2018.
73 Y. Tan, K. Zhu, D. Li, F. Bai, Y. Wei and P. Zhang, *Chem. Eng. J.*, 2014, **258**, 93–100.
74 M. S. Y. Parast and A. Morsali, *Inorg. Chem. Commun.*, 2011, **14**, 645–648.
75 S. Geranmayeh and A. Abbasi, *J. Inorg. Organomet. Polym. Mater.*, 2013, **23**, 1138–1144.
76 P. Mahata, T. Aarthi, G. Madras and S. Natarajan, *J. Phys. Chem. C*, 2007, **111**, 1665–1674.

 This journal is © The Royal Society of Chemistry 2015

Published on 12 December 2014. Downloaded by Changchun Institute of Optics, Fine Mechanics and Physics, CAS on 29/05/2016 14:28:41.

77 H. Guo, T. Li, W. Chen, L. Liu, X. Yang, Y. Wang and Y. Guo, *Nanoscale*, 2014, **6**, 15168–15174.
78 P. Mahata, D. Sarma, C. Madhu, A. Sundaresen and S. Natarajan, *Dalton Trans.*, 2011, **40**, 1952–1960.
79 D. Sarma, P. Mahata and S. Natarajan, *Curr. Sci.*, 2012, **103**, 1185–1192.
80 A. Kong, Q. Lin, C. Mao, X. Bu and P. Feng, *Chem. Commun.*, 2014, **50**, 15619–15622.
81 H. Zhao, H. Song, L. Xu and L. Chou, *Appl. Catal., A*, 2013, **456**, 188–196.
82 F.-X. Qin, S.-Y. Jia, Y. Liu, X. Han, H.-T. Ren, W.-W. Zhang, J.-W. Hou and S.-H. Wu, *Mater. Lett.*, 2013, **101**, 93–95.
83 A. Banerjee, U. Singh, V. Aravindan, M. Srinivasan and S. Ogale, *Nano Energy*, 2013, **3**, 1158–1163.
84 L. Hu, B. Qu, C. Li, Y. Chen, L. Mei, D. Lei, L. Chen, Q. Li and T. Wang, *J. Mater. Chem. A*, 2013, **1**, 5596.
85 D. Xie, Q. Su, Z. Dong, J. Zhang and G. Du, *CrystEngComm*, 2013, **15**, 8314.
86 S. Kim, K. W. Dawson, B. S. Gelfand, J. M. Taylor and G. K. Shimizu, *J. Am. Chem. Soc.*, 2013, **135**, 963–966.
87 M. Sadakiyo, T. Yamada and H. Kitagawa, *J. Am. Chem. Soc.*, 2009, **131**, 9906–9907.
88 W. Lu, X. Qin, A. M. Asiri, A. O. Al-Youbi and X. Sun, *Analyst*, 2013, **138**, 429–433.
89 X. W. Lou, D. Deng, J. Y. Lee and L. A. Archer, *J. Mater. Chem.*, 2008, **18**, 4397.
90 P. Horcajada, S. Surble, C. Serre, D. Y. Hong, Y. K. Seo, J. S. Chang, J. M. Greneche, I. Margiolaki and G. Ferey, *Chem. Commun.*, 2007, 2820–2822.
91 R. Jasinski, *Nature*, 1964, **201**, 1212–1213.
92 M. Lefèvre, E. Proietti, F. Jaouen and J.-P. Dodelet, *Science*, 2009, **324**, 71–74.
93 T. Palaniselvam, B. P. Biswal, R. Banerjee and S. Kurungot, *Chem.–Eur. J.*, 2013, **19**, 9335–9342.
94 P. Su, H. Xiao, J. Zhao, Y. Yao, Z. Shao, C. Li and Q. Yang, *Chem. Sci.*, 2013, **4**, 2941.
95 W. Schmitt, J. P. Hill, S. Malik, C. A. Volkert, I. Ichinose, C. E. Anson and A. K. Powell, *Angew. Chem.*, 2005, **44**, 7048–7053.
96 G. Mao, W. Dong, D. G. Kurth and H. Möhwald, *Nano Lett.*, 2004, **4**, 249–252.